SWBSS
2011 19 - 22 October
Limassol, Cyprus

Salt Weathering on Buildings and Stone Sculptures

Editors:
I. Ioannou & M. Theodoridou

EDITORS:

Ioannis Ioannou, PhD
University of Cyprus
Department of Civil and Environmental Engineering
Building Materials & Ledra Laboratories
PO Box 20537
1678 Nicosia
Cyprus
ioannis@ucy.ac.cy

Magdalini Theodoridou, PhD
University of Cyprus
Department of Civil and Environmental Engineering
Building Materials & Ledra Laboratories
PO Box 20537
1678 Nicosia
Cyprus
mtheodo@ucy.ac.cy

ISBN 978-9963-7355-1-8

Quantitative analysis of saline transport and crystallization damage in porous limestone visualized by neutron and X-ray imaging

Derluyn H.[1,2*] Griffa M.[2], Mannes D.[3], Jerjen I.[2], Dewanckele J.[4], Vontobel P.[3], Derome D.[2], Cnudde V.[4], Lehmann E.[3] and Carmeliet J.[1,2]
[1] Chair of Building Physics, ETH Zürich, Zürich, Switzerland
[2] Swiss Federal Laboratories for Materials Science and Technology, EMPA, Dübendorf, Switzerland
[3] Spallation Neutron Source, PSI, Villigen, Switzerland
[4] Department of Geology and Soil Science - UGCT, Ghent University, Gent, Belgium
*corresponding author´s email: derluyn@arch.ethz.ch

ABSTRACT

This article presents coupled data on saline transport, pore filling due to salt crystallization and resulting salt damage in Savonnières limestone. This is achieved by combining the non-destructive techniques of neutron radiography - for transport imaging - and X-ray microtomography - for pore structure and fracture visualization – applied to the same sample when subjecting it to consecutive wetting-drying cycles. Capillary uptake of water, 1.4m sodium sulfate and 5.8m sodium chloride solutions is studied at 25°C. An important decrease of the penetration coefficient for the salt solutions compared to water is found. Halite crystallization fronts are located based on neutron radiographs of the dried samples. Porosity analysis of the X-ray tomographic datasets quantifies pore filling at the position of the crystallization front. The damaging character of the salts is assessed from these datasets too. Only the sodium chloride wetted samples show fractures under the specific test conditions used (drying at 40°C).

Keywords: neutron radiography, X-ray tomography, saline transport, pore filling, crystallization damage

1 INTRODUCTION

Combining information on respectively saline transport, pore filling and fracturing due to salt crystallization will enhance the understanding of the coupling between transport and mechanical processes related to salt weathering. This will improve our knowledge required for the selection of the best suited materials and conservation methods for civil constructions and our cultural heritage. Additionally, such a dataset can advance numerical modeling of crystallization in porous media as these data are indispensable for its validation.

Therefore an experimental study was conducted on samples of Savonnières limestone which were subjected to repeated wetting-drying cycles. Repeated uptake of salt solution was performed in order to accumulate an amount of salt inside the material sufficient to induce fracturing. Non-destructive techniques were needed to allow repeated testing of the same sample. We achieved this goal by combining neutron imaging with X-ray micro computed tomography (μCT). As hydrogen highly attenuates neutron radiation propagation, transmission-based neutron imaging is a well suited technique to study hydrogenous liquid transport. The higher resolution achievable with X-ray μCT allows for assessing porosity changes and fracture

formation due to salt crystallization. By applying both techniques on the same sample, we could gain threefold data on liquid transport, pore filling and fracturing processes. The aim of this study was to get high quality images from which good quantitative data could be derived.

In the first part of this article, the sample preparation, the two imaging techniques and the applied image analysis methods are described. The results are presented in the second part. First the difference between water and saline uptake of sodium sulfate and sodium chloride solution is quantified. Then the transport in samples which underwent different wetting-drying cycles is presented and the corresponding pore filling and crystallization damage is assessed.

2 METHODOLOGY

2.1 Materials

The type of stone studied is Savonnières limestone, a French layered oolitic limestone. This stone is widely available and is typically used for restoration projects (Dreesen & Dusar 2004). Savonnières limestone is a quasi-pure calcitic stone, without clay minerals. Remarkable are the hollow, dissolute cores of the oolites. The pore system shows both micro (0.1 - 10 μm) - and macropores (100 μm range) (Roels 2000). For the capillary uptake tests, square prisms of 10 x 10 mm^2 base and 15 mm height were used, with the bedding direction of the stone parallel to the base. A hydrophobic treatment was applied on their top side (SILRES® BS 280, WACKER) and they were sealed on the circumferential sides by a liquid and vapour tight membrane (aluminum tape, which is quasi transparent to neutrons). The hydrophobic treatment was applied with a paint brush and penetrated the top of the stone over a depth of 2 to 3 mm. The aluminum tape ensured that no transport occurred through the circumferential sides. From the bottom side, the samples could be brought into contact with a free water or salt solution surface, after which capillary uptake occurred. After this uptake, the bottom side was also sealed (water and vapour tight) with tape. Thus, drying could only occur through the hydrophobically treated top side.

As the hydrophobic treatment prevented liquid transport, only vapour diffusion could occur through the treated pores. The treatment prevented salt efflorescence and induced in-pore crystallization. The confined crystallization caused a buildup of interior stresses and a higher risk for fracturing of the material. This process was desired as the study aimed at collecting combined data on transport and damage within a limited time frame. Additionally, the accumulated amount of salt could be controlled by weight monitoring without the problem of material loss, as efflorescence did not occur. The application of a hydrophobic treatment is also of practical interest as it is commonly applied on building materials for conservation purposes. However, such treatments often increase the risk for salt damage (Ioannou & Hoff 2008).

We measured capillary uptake with water, sodium sulfate and sodium chloride solution. Sodium sulfate and sodium chloride are two of the most damaging salts mentioned in literature (Goudie & Viles 1997). Sodium sulfate has two stable phases - mirabilite ($Na_2SO_4.10H_20$) and thenardite V ($Na_2SO_4(V)$) - and two metastable phases - heptahydrate ($Na_2SO_4.7H_20$) and thenardite III ($Na_2SO_4(III)$). Sodium chloride has one stable crystal phase above the freezing point: halite (NaCl). By cooling a sodium sulfate solution below room temperature, mirabilite or heptahydrate may form, while by drying, thenardite may also precipitate. Crystallization of halite can only be induced by drying. The wetting of our samples took place at 25°C using 1.4m Na_2SO_4-solution or 5.8m NaCl-solution. Subsequently, the samples were dried at 40°C under dry air conditions (± 5% RH), so thenardite and halite precipitation were expected.

2.2 Neutron radiography

Capillary uptake experiments were performed at the NEUtron Transmission RAdiography (NEUTRA) beam-line of the Paul Scherrer Institute (PSI), Switzerland. This beamline is fed by

the Swiss Neutron Spallation Source (SINQ) and is operated with neutrons within a thermal spectrum characterized by a Maxwell-like probability density function, with a most probable energy level of about 25 meV (Lehmann et al. 2001). Fig. 1 shows the experimental setup inside NEUTRA and a schematic overview of the neutron beamline. The setup contained a small sample holder, a custom-made elevator, supporting a container which was remotely controlled from outside the beamline, a neutron detector and high density boronated polyethylene blocks to shield the elevator against neutron radiation, in order to avoid building up radioactivity of the setup components. High density boronated polyethylene shows a large scattering and absorption of neutrons, making it a perfect body opaque to neutron radiation. The X and Y axes in Fig. 1 correspond to the detector plane while the Z axis is aligned to the neutron beam direction, orthogonal to the detector plane. The detector consisted of a scintillator-CCD camera-system, with a total field of view of 87 mm lateral size. The scintillator was a plane slab of ZnS crystal, doped with ^{6}Li as neutron absorbing agent and 100 µm thick. The scintillator converted the neutrons into visible light photons. The photons were then led via a mirror onto a cooled 16-bit CCD camera (1024 x 1024 pixels). The exposure time was 8 seconds per radiography.

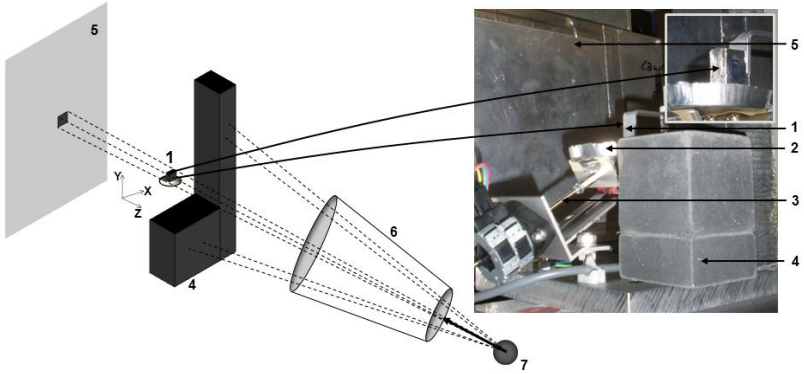

Figure 1. a) Schematic overview of the experimental setup inside the NEUTRA beamline: (1) sample holder, (2) water container, (3) remote control elevator, (4) boron block for shielding, (5) detector in the background, (6) collimator and (7) neutron source.

A reference radiograph of the initial dry sample was taken right after the sample was placed on the sample holder and before it was in contact with water/salt solution. Then the filled container was remotely moved up until the base of the sample was in contact with the free liquid surface. From then on, radiographs were acquired at 24 seconds intervals, over a period of 60 to 180 minutes depending on the uptake rate of the different samples. As a control reference, the total mass of intruded water/salt solution was determined by measuring the sample weight on a balance before and after the capillary uptake test.

The radiographs were corrected for artifacts using the Quantitative Neutron Imaging (QNI) method developed by Hassanein et al. (Hassanein et al. 2005, Hassanein 2006). This method includes corrections for neutron scattering and considers the polychromatic character of the beam. The scattering correction is based on Monte-Carlo simulations of the main scattering component within the NEUTRA setup. The QNI method results in a corrected transmission value T^{corr} which can be described by the exponential law of attenuation (Beer-Lambert law):

$$T^{corr}(t) = \exp\left(-\mu_{eff} \cdot d\right) \tag{1}$$

with μ_{eff} the effective attenuation coefficient and d the thickness of the main scattering component, which is in our experiments water or salt solution. The μ_{eff}-values at a concentration of 1.4m and 5.8m were used for the Na_2SO_4-solution and NaCl-solution, respectively. The corrected wet transmission contains information on the stone material and the liquid:

$$T_{wet}^{corr}(t) = \exp\left(-\mu_{eff} \cdot \left(d_{s,l} + d_l(t)\right)\right) \tag{2}$$

with d_l the thickness of the liquid phase and $d_{s,l}$ the stone thickness quantified as if it were also liquid. To find the correct liquid content, we referenced the wet state to the corrected transmission image of the dry sample:

$$T_{dry}^{corr} = \exp\left(-\mu_{eff} \cdot d_{s,l}\right) \tag{3}$$

The corresponding moisture content (in kg/m^3) equals then:

$$w_l(t) = \rho_l \frac{d_l(t)}{d_s} = -\frac{\rho_l}{\mu_{eff} \cdot d_s} \ln\left(\frac{T_{wet}^{corr}(t)}{T_{dry}^{corr}}\right) \tag{4}$$

with ρ_l the density of the liquid and d_s the real sample thickness.

Considering that the moisture transport was mainly 1D (in the y-direction), the moisture content at every height y could be calculated by averaging over the width of the sample. This provides moisture content profiles in the sample with time. We mainly visualized the first uptake phase which is driven by capillary forces and can be approximated as (Hall & Hoff 2002):

$$l(t) = B \cdot \sqrt{t} \tag{5}$$

with *l* the position of the (sharp) moisture front, and *B* the penetration coefficient. As the front is not strictly sharp (see Fig. 2), *l(t)* was derived from the moisture profiles as the position at which the moisture content equals half of the maximal content. The penetration coefficient is a constant value, expressing the capacity of the medium to absorb a certain liquid by capillarity, found by calculating the slope of the first part of the *l(t)*-$\sqrt{t}$ curve.

2.3 X-ray microtomography

We acquired X-ray tomographic datasets of the initial samples before wetting and after the last wetting-drying cycle, when they had completely dried out (called 'weathered' sample). The samples were measured with an X-ray micro tomography cone beam setup consisting of a μm spot size X-ray tube "XT9160-TXD" from Viscom, a rotation table "UPR-160F air" from Micos and an X-ray flat panel detector "C7942 CA02" from Hamamatsu. A voltage of 80 kV was applied to accelerate the electrons which impacted on a diamond target. On the target, the electron beam had a power in the order of one Watt and the focus size was ~2 μm. The samples were mounted on the rotation table 70 mm away from the X-ray source and the distance between the source and the detector was 500 mm. 721 projection radiographs, each with 1120x1184 pixels, were acquired at angles uniformly distributed over 2π, whereby the last projection served as a check for the quality of the measurement (the projections at 0 and 2π should be equal). The total integration time for each projection radiograph was 4 s. In order to correct for dark counts (background noise of the CCD camera) and inhomogeneities of the detector a dark and a flat image were acquired with total integration time of 32 s and 64 s, respectively. The projection radiographs were corrected for bad pixels, beam hardening and ring artifacts before a standard filtered backprojection algorithm was used for reconstructing the 1120x1120x1184 3D absorption tomographic datasets (Feldkamp et al. 1984). Considering the detector pixel size of 100 μm (2x2 binned) and the magnification of 500/70 = 7.14, the voxel lateral size of the reconstructed 3D volume resulted to be 14 μm, which is larger than the focal spot size and ensured that the image is not blurred.

A visual comparison of the initial and the weathered datasets was made to assess damage in the sample. In a second step, the datasets were compared for their porosity change due to the wetting-drying cycles using the Morpho+ software from the Centre for X-ray Tomography at the Ghent University (UGCT) (Brabant et al. 2011). First the datasets of the weathered and the initial sample were aligned by visually comparing the positions of the non-damaged part. This to assure that the same slices of the initial and the weathered dataset were compared when doing quantitative analysis on the non-damaged part. The datasets were filtered in Morpho+ to improve the signal-to-noise ratio, using the bilateral filter. Then dual thresholding was applied by manually selecting the grayscale interval on the image's histogram. This created binary datasets representing the pore space. From this, the porosity distribution over the height of the sample was calculated, within the limits of the obtained resolution. This means that only the macroporosity of the hollow oolites and the intergranular pores could be accounted.

3 RESULTS

3.1 Neutron radiography

8 samples visualized in NEUTRA were analyzed with the QNI method. A general overview is given in Table 1. The final mass of water or salt solution taken up, as determined from the image analysis and from weighing on the balance, is given. A difference up to only 3% is found (except for sample S7 where the difference is higher due to fluctuations in the measurement results). The QNI correction procedure was needed to achieve a good quantification of the moisture mass, without it differences up to 15% were observed.

Table 1. Overview of the samples visualized in NEUTRA, the analyzed uptake, the final uptaken liquid masses determined from neutron images (using QNI) m_N and from balance measurements m_B, the difference between both and the penetration coefficient B.

sample	uptake	m_N [mg]	m_B [mg]	difference: $(m_N-m_B)/m_B$ [weight%]	B [mm/s$^{1/2}$]
S1	water	211	211	0.0	0.34
S1	Na_2SO_4 – cycle 1	199	202	-1.6	0.24
S2	water	170	170	-0.3	0.28
S2	NaCl – cycle 1	187	184	1.5	0.21
S3	water	216	216	0.0	0.31
S4	water	204	199	2.7	0.64
S5	Na_2SO_4 – cycle 2	185	188	-1.4	0.29
S6	Na_2SO_4 – cycle 3	140	140	0.6	0.38
S7	NaCl – cycle 3	208	183	13.6	0.22
S8	NaCl – cycle 4	194	193	0.4	0.18

4 samples (S1 to S4) were wetted first with water. The 2D moisture distribution of sample S1 as resulting from the image analysis is given for 3 time steps in Fig. 2a-c. Fig. 2c shows that the hydrophobic treatment on the top side prevents liquid flow to the outer top of the sample. The corresponding moisture profiles are given in Fig. 2d. From these, the moisture fronts were calculated. The result for the water wetted samples is given in Fig. 3a. Samples S1 to S3 show a similar penetration coefficient, whereas sample S4 has a much faster water infiltration. This is explained by its pore structure, which can be assessed by the X-ray tomographic dataset of this sample (see Fig. 4a). Samples S1 to S3 represent the main pore structure of Savonnières limestone. In addition layers consisting of small bivalve shell moulds can be observed in some parts of the stone, which is clearly the case for sample S4. They act as preferential flow channels during moisture uptake, as was also observed by Roels (2000).

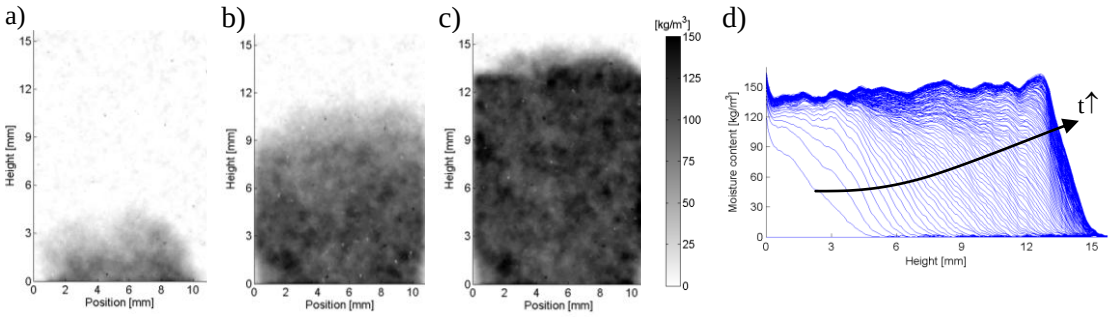

Figure 2. 2D moisture distribution in sample S1 during water uptake at a) 24 s, b) 604 s, c) 3020 s and d) the corresponding moisture profiles over the height.

After complete drying, sample S1 is wetted with 1.4m sodium sulfate solution and sample S2 with 5.8m sodium chloride solution. In this way, a clear comparison can be made between water and salt solution imbibition, as the measurements are done on the same sample. It is found that the water uptake is faster than the salt solution uptake and that the ratio $B_{salt\ sol}/B_{water}$ amounts 0.71 with sodium sulfate uptake and 0.75 with sodium chloride uptake. According to Washburn

(1921) the part of the penetration coefficient dependent on the liquid type is proportional to $\sqrt{\sigma/\eta}$, with σ the surface tension and η the viscosity. This means that $B_{salt\ sol}/B_{water}$ equals $\sqrt{(\sigma_{salt\_sol} \cdot \eta_{water})/(\eta_{salt\_sol} \cdot \sigma_{water})}$. At 25°C the viscosity of water is 0.89 mPa.s, of 1.4m sodium sulfate solution 1.64 mPa.s (Korosi et al. 1968), and of 5.8m sodium chloride solution 1.69 mPa.s (Kestin et al. 1981). The surface tension for water is 72 mN/m, for the sodium sulfate solution it is estimated to be 77 mN/m (Shahidzadeh-Bonn et al. 2010) and for the sodium chloride solution 80 mN/m (Ali et al. 2006). For both salt solutions the ratio $B_{salt\ sol}/B_{water}$ is 0.76, very close to the ratios obtained from the neutron measurements, thus confirming their validity.

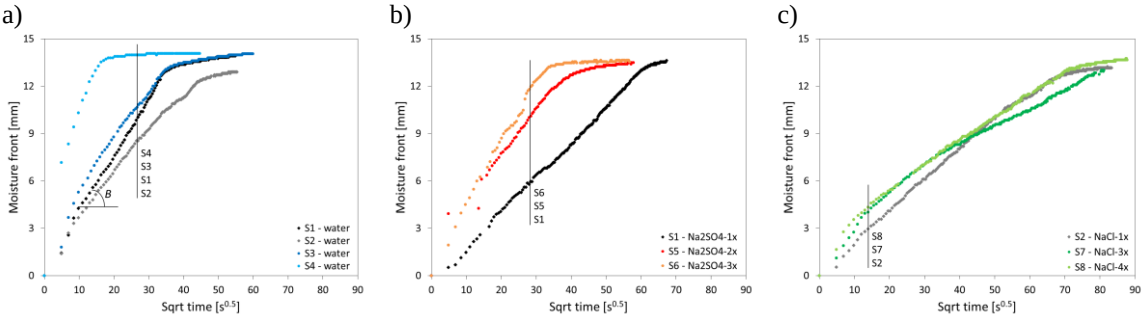

Figure 3. Moisture fronts in function of square root of time for samples wetted with a) water, b) 1.4m Na_2SO_4-solution, c) 5.8m NaCl solution. The penetration coefficient *B* is determined by the curve's slope.

Four samples already underwent wetting-drying cycles before going to NEUTRA, for these samples only the 2nd (S5), 3th (S6, S7) or 4th (S8) capillary uptake was imaged. The crystallization front of sodium chloride wetted samples can be clearly seen in the neutron radiograph of the dry state (Fig. 4c). As chlorine attenuates the neutron beam more than the calcite stone, the location of the NaCl crystals shows up darker than the stone material. The crystallization front is located at the upper part of the samples, just below the hydrophobic treated zone. For sodium sulfate wetted samples the crystallization front cannot be visualized in the neutron radiographs as the attenuation difference between sodium sulfate and stone is very small. However, we expect the crystallization front to be at the similar location.

The sodium chloride wetted samples S7 and S8 show the same slow uptake of the 5.8m salt solution as in sample S2 (Fig. 2c), illustrating the repeatability of the test when working with alike samples. Sample S5 and S6 show a faster uptake than sample S1 (Fig. 2b). The reason for this is that sample S5 contains bivalve shell moulds forming preferential flow channels, as in sample S4. Sample S6 had not completely dried out before doing the uptake test in NEUTRA, causing the observed faster uptake.

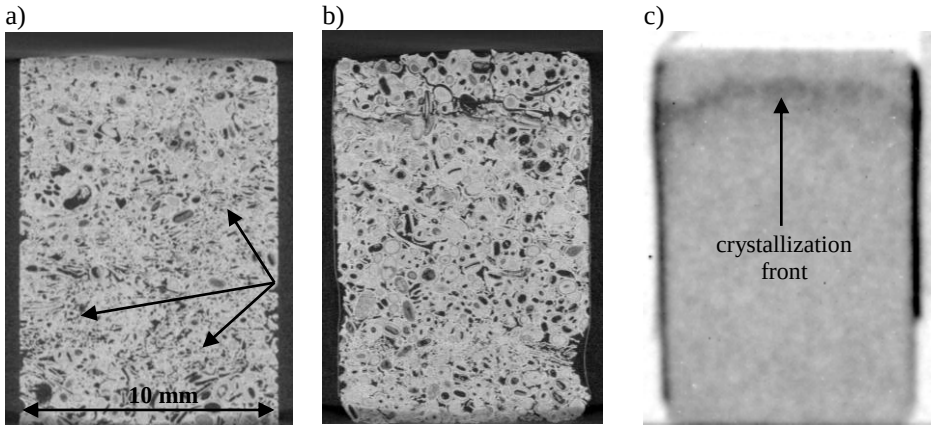

Figure 4. Vertical cross section of X-ray tomography of a) sample S4, containing bivalve shell moulds, b) sample S7 after the 4th wetting-drying cycle. c) Neutron transmission image of sample S7 after 2 wetting-drying cycles.

3.2 X-ray microtomography

The X-ray tomographic datasets of all initial and weathered samples have been visually compared: the three samples wetted with sodium sulfate (S1, S5, S6) show no damage, all three samples wetted with sodium chloride (S2, S7, S8) show fractures. The main fracture is located at the upper part of the samples underneath the hydrophobic treated zone and is formed over the whole cross section of the sample (Fig. 4b). Additionally some secondary fractures are observed propagating to the upper surface. The position of the main fracture corresponds to the crystallization front observed from the neutron radiographs (Fig. 4c).

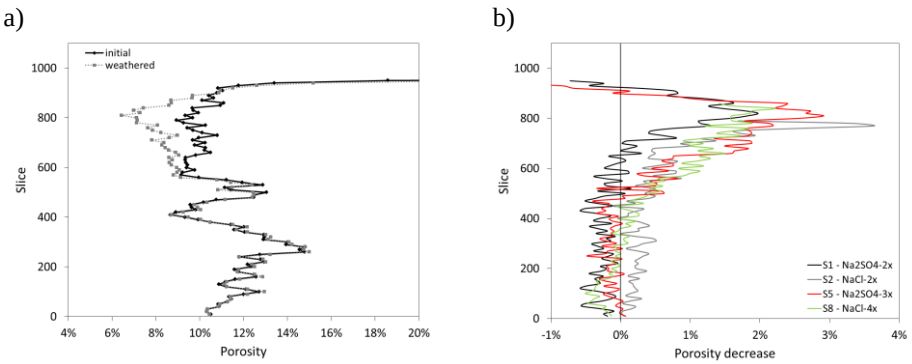

Figure 5. a) The porosity of sample S5 in the initial and weathered state as analyzed in Morpho+, b) the absolute porosity decrease of samples S1, S2, S5 and S8 after several wetting-drying cycles.

Four samples have been quantitatively analyzed: S1, S2, S5 and S8. S1 and S2 underwent in total two wetting-drying cycles, S5 three and S8 four. The weathered X-ray tomographic dataset was acquired after completing the final drying. The porosity of the initial and the weathered sample was compared by calculating the partial porosity of blocks of 10 slices over the height of the sample (e.g. for sample S5 in Fig. 5a). The difference between both results gives the porosity decrease as shown in Fig. 5b, indicating a filling of the pores in the upper part of the weathered sample where the salt crystals are precipitated. We remark that for the fractured samples S2 and S8 the upper fractured part of the sample is removed from the analysis, as the corresponding slices from the weathered tomographic dataset are shifted with respect to the initial tomographic dataset due to the fracture displacements.

4 CONCLUSIONS & OUTLOOK

We can conclude that the combination of the two imaging techniques together with their quantitative analysis can provide a complete dataset of coupled information on saline transport and fracturing due to salt crystallization in porous materials. The advantages of using both techniques on the same sample are clearly illustrated: differences in water uptake shown in the neutron image analysis can be explained based on knowledge of the pore structure derived from the X-ray tomographic datasets (e.g. for sample S4). Halite crystallization fronts can be visualized from the neutron radiographs, porosity analysis of the tomographic datasets confirms the position of these crystallization fronts and also indicates thenardite crystallization fronts. The neutron imaging allows for quantifying the slower uptake of saline solutions compared to water. The X-ray tomographic datasets reveal that under the specific applied test conditions (wetting at 25°C, drying at 40°C), halite is clearly damaging the Savonnières limestone, whereas thenardite formation seems to be less harmful. Although no fractures were observed in the sodium sulfate wetted samples discussed in this article, another sample series used for follow-up measurements showed fracturing after several wetting-drying cycles with sodium sulfate solution.

Further research will focus first on the analysis of the neutron radiographs of rewetting cycles

following the capillary uptake presented here of the samples S1, S2, S5 and S7. Secondly, neutron images of drying of water and salt solution wetted samples, visualized at higher resolution in the ICON beamline at PSI, will be analyzed. The X-ray tomographic datasets will be processed further to see if we can reveal more information about the salt precipitation and additional experiments will be planned to assess why sodium chloride seems more damaging than sodium sulfate in our test case.

5 ACKNOWLEDGEMENTS

The technical help of R. Vonbank and S. Carl (EMPA) and J. Hovind (PSI) are greatly acknowledged. The assistance of M. Abuku, M. Gilani, S. Hansen, P. Moonen, A. Patera, S. Saneinejad, F. Voisard and T. Wangler are greatly appreciated. IWT-Flanders is acknowledged for its grant to J. Dewanckele.

REFERENCES

ALI, K., ANWAR-UL-HAQ, BILAL, S., SIDDIQI, S., 2006. Concentration and temperature dependence of surface parameters of some aqueous salt solutions, *Colloids and Surfaces A: Physicochemical and Engineering Aspects*, 272, 105-110.

BRABANT, L., VLASSENBROECK, J., DE WITTE, Y., CNUDDE, V., BOONE, M.N., DEWANCKELE, J., VAN HOOREBEKE, L., 2011. Three-dimensional analysis of high-resolution X-ray computed tomographydata with Morpho+, *Microscopy and Microanalysis*, 17(2), 252-263.

DREESEN, R., DUSAR, M., 2004. Historical building stones in the province of Limburg (NE Belgium): role of petrography in provenance and durability assessment, *Materials Characterization*, 53, 273-287.

FELDKAMP, L.A., DAVIS, L.C., KRESS, J.W., 1984. Practical cone-beam algorithm, *Journal of Optical Society of America*, 1(6): 612-619.

GOUDIE, A., VILES, H., 1997. *Salt Weathering Hazards*, Wiley, Chichester.

HALL C, HOFF WD., 2002. *Water transport in brick, stone and concrete*, Spon Press, New York.

HASSANEIN, R., LEHMANN, E., VONTOBEL, P., 2005. Methods of scattering corrections for quantitative neutron radiography, *Nuclear Instruments and Methods in Physics Research Section A*, 542, 353-360.

HASSANEIN, R., 2006. *Correction methods for the quantitative evaluation of thermal neutron tomography*. Thesis (PhD), ETH Zurich.

IOANNOU, I., HOFF, W.D., 2008. Water repellent influence on salt crystallization in masonry, *Proceedings of ICE, Construction Materials*, 161, 17-23.

KESTIN, J., EZZAT KHALIFA, H., CORREIA, R.J., 1981. Tables of the dynamic and kinematic viscosity of aqueous NaCl solutions in the temperature range 20-150°C and the pressure range 0.1-35 MPa, *Journal of Physical and Chemical Reference Data*, 10(1), 71-87.

KOROSI, A., FABUSS, B.M., 1968. Viscosities of binary aqueous solutions of NaCl, KCl, Na_2SO_4, and $MgSO_4$ at concentration and temperatures of interest in desalination processes, *Journal of chemical and engineering data*, 13(4), 548-552.

LEHMANN, E.H., VONTOBEL, P., WIEZEL, L., 2001. Properties of the Radiography Facility NEUTRA at SINQ and its Potential for Use as European Reference Facility, *Nondestructive Testing and Evaluation*, 16, 191–202.

ROELS, S., 2000. *Modelling unsaturated moisture transport in heterogeneous limestone*. Thesis (PhD), K.U.Leuven.

SHAHIDZADEH-BONN, N., DESARNAUD, J., BETRAND, F., CHATEAU, X., BONN, D., 2010. Damage in porous media due to salt crystallization, *Physical Review E*, 81, 066110.

WASHBURN, E.W., 1921. The dynamics of capillary flow, *Physical review*, 17(3), 273-283.